

# Reversing Cancer Multidrug Resistance in Xenograft Models via Orchestrating Multiple Actions of Functional Mesoporous Silica Nanoparticles

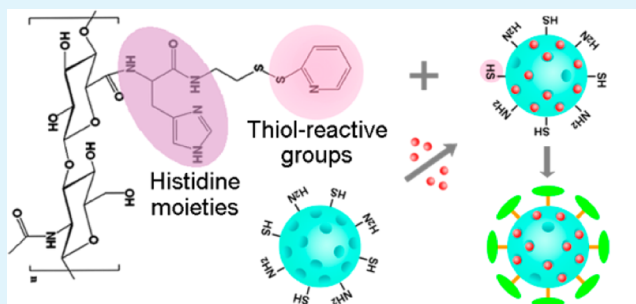
Debin Yang, Tingfang Wang, Zhigui Su,\* Lingjing Xue, Ran Mo, and Can Zhang\*

State Key Laboratory of Natural Medicines, Jiangsu Key Laboratory of Drug Discovery for Metabolic Diseases, Center of Advanced Pharmaceuticals and Biomaterials, China Pharmaceutical University, Nanjing 210009, China

## S Supporting Information

**ABSTRACT:** A multistimuli responsive drug delivery system (DDS) based on sulfhydryl and amino-cofunctionalized mesoporous silica nanoparticles (SH/NH<sub>2</sub>-MSNs) has been developed, in which the multifunctional hyaluronic acid (HA) derivatives were grafted onto the SH/NH<sub>2</sub>-MSNs by disulfide bonds for targeting delivery, controlling drug release and reversing multidrug resistance (MDR). The doxorubicin (Dox) loaded multifunctional HA derivatives modified mesoporous silica nanoparticles (Dox/HHS-MSNs) were enzyme and redox sensitive, which could respond to the intracellular stimuli of hyaluronidase (HAase) and glutathione (GSH) successively and prevent drug leakage before reaching the tumor tissues. The cellular uptake experiments showed that Dox/HHS-MSNs were vulnerable to be endocytosed into the Dox-resistant human breast adenocarcinoma (MCF-7/ADR) cells, efficiently realized the endolysosomal escape and remained in the cytoplasm. Because of orchestrating multiple actions above including active targeting, endolysosomal escape and efficient multilevel drug release, Dox/HHS-MSNs could induce the strongest apoptosis and cytotoxicity of MCF-7/ADR cells. Furthermore, a series of *in vivo* studies on MCF-7/ADR tumor-bearing xenograft mouse models demonstrated that Dox/HHS-MSNs possessed the enhanced tumor-targeting capacity and the best therapeutic efficacy to reverse cancer MDR.

**KEYWORDS:** mesoporous silica nanoparticles, multidrug resistance, enzyme and redox sensitive, endolysosomal escape, active targeting, multilevel drug release



## 1. INTRODUCTION

Cancer as one kind of devastating diseases with complicated etiopathogenesis is a serious threat to human health worldwide.<sup>1</sup> Chemotherapy is a well-known therapeutic option for clinical cancer treatment,<sup>2</sup> but frequently encounters failure due to the occurrence of multidrug resistance (MDR),<sup>3</sup> which can be intrinsic or acquired in most cancers with numerous mechanisms.<sup>4</sup> For example, the overexpression of P-glycoprotein (P-gp) is a well-known phenotype in lots of MDR cells, which can excrete the free drug out of cells.<sup>5</sup> To achieve targeted therapeutic concentration, higher dosage should be given but that means greater toxic side effects on normal tissues.<sup>6</sup>

To address this dilemma, great attempts have been made to exploit the nanoparticle-based drug delivery systems (DDSs) for overcoming the MDR in cancer therapy.<sup>7–9</sup> Although considerable achievements have been acquired, there are still many deficiencies, among which the poor cellular uptake and insufficient drug release inside cells are two hurdles to circumvent MDR because they can induce a low intracellular drug concentration below the therapeutic window.<sup>7,10</sup> Therefore, an ideal DDS requires not only the capacity of active targeting but also the sensitivity of drug release in accordance with the

environmental stimuli at the specific target sites. These stimuli involve the intrinsic physiological differentiation, such as pH,<sup>11</sup> redox potential,<sup>12</sup> enzymes<sup>13</sup> and ATP levels,<sup>14</sup> as well as a series of external factors, such as temperature,<sup>15</sup> light,<sup>16</sup> ultrasound,<sup>17</sup> magnetic fields,<sup>18</sup> and electric current.<sup>19</sup> Among them, redox potential as an internal stimulus has been widely used based on the gradient of reduced glutathione (GSH), which presents an extremely higher concentration in subcellular compartments and cytosol (1–10 mM) than that in extracellular fluids (2–20 μM).<sup>20</sup> Moreover, the GSH level in tumor cytosol is at least 3-fold higher than that in normal cells,<sup>20</sup> rendering the redox-responsive DDSs available for specific release inside tumors.<sup>21</sup> Beyond the above two points, another critical factor of reversing cancer MDR for DDSs is successful and rapid escape from endosomes and lysosomes (endolysosomes), where various catabolic enzymes store and the nanocarriers are stranded initially.<sup>22</sup> The longer trapping time in that for

Received: April 24, 2016

Accepted: July 15, 2016

Published: July 15, 2016

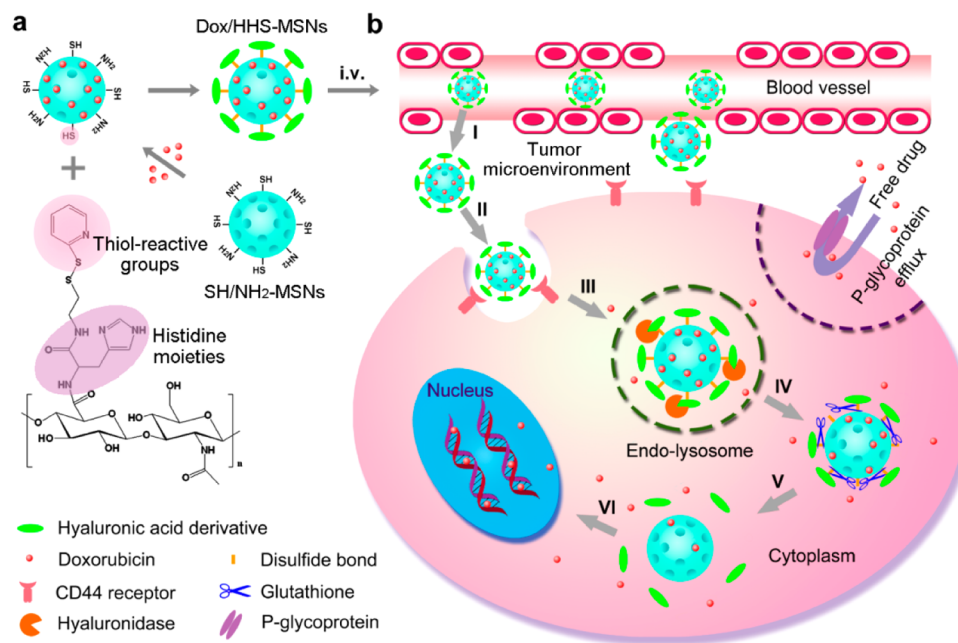
most nanoparticles and drugs the more unfavorable to cancer therapy.<sup>6</sup>

Among the numerous DDSs, mesoporous silica nanoparticles (MSNs) have attracted tremendous interests on account of their excellent features including the tunable pore sizes (2–50 nm), large specific surface areas, good biocompatibility and particularly the convenience of surface functionalization.<sup>23</sup> The chemotherapeutic drug is generally encapsulated into the pores of MSNs based on the capillary action or specific interaction with the inner groups. To control the drug release effectively, intelligent MSNs are achieved by immobilization of functional capping agents onto the surface of MSNs. These capping agents can be various inorganic nanoparticles, such as quantum dots,<sup>24</sup> gold nanoparticles,<sup>25</sup> graphene<sup>26</sup> and magnetic nanoparticles,<sup>27</sup> as well as organic (bio)molecules and (bio)macromolecules, such as peptide,<sup>28</sup> lipid bilayers,<sup>29</sup> polymers,<sup>30</sup> cyclodextrin,<sup>31</sup> and collagen.<sup>32</sup> To target the specific sites, multifarious targeting ligands, such as folic acid,<sup>33</sup> TAT peptide<sup>34</sup> and triphenylphosphonium (TPP)<sup>22</sup> are decorated on the capping agents or directly on MSNs. In this study, we selected the synthetic hyaluronic acid (HA) derivatives (HA-His-SS-Py), which were functionalized with histidine moieties and thiol-reactive groups, as the capping agent to construct an intelligent MSN-based DDS. HA is a naturally occurring anionic glycosaminoglycan with biodegradable, biocompatible, low toxic and nonimmunogenic characters.<sup>35–37</sup> Intriguingly, it has been widely used for DDSs in cancer research mainly due to its specific interaction with some receptors overexpressed on several cancer cell membranes, like CD44 and RHAMM.<sup>38</sup> Furthermore, HA can be degraded to smaller fragments under hyaluronidase (HAase), which is abundant in many tumor matrices and intracellular organelles including endolysosomes.<sup>39</sup> Besides with the virtues

of HA, our synthetic HA derivatives provides a particular function of facilitating the endolysosomal escape of prepared nanoparticles to realize their cytoplasmic delivery, which was attributed to the proton buffering capacity of histidine moieties.<sup>40</sup> It is necessary to emphasize that different polymer shells with distinct functions are considered to play important roles in improving the biodistribution of MSN-based DDSs and reversing the cancer MDR.<sup>41,42</sup> Although there have been some reports about the DDSs based on HA conjugated MSNs for cancer therapy,<sup>43–45</sup> just one stimulus was mostly studied and the endolysosomal escape behavior was not reported, which was an important concern for intracellular delivery of anticancer drugs. And compared to the multistimuli responsive DDSs, only one single signal sensitive DDSs reduced the opportunities of overcoming MDR and development of highly customizable therapies. Based on the above consideration, the novel MSN-based DDS orchestrating multiple functions of active targeting, endolysosomal escape, enzyme and redox sensitivities was constructed and investigated.

Herein, we reported an enzyme and redox dual-responsive DDS as shown in Scheme 1, which could significantly reverse the MDR phenomenon in consequence of the enhanced cellular uptake, rapid endolysosomal escape and sufficient intracellular multilevel drug release. This multistimuli responsive DDS was constructed by integrating the two modules, HA-His-SS-Py and Dox-loaded sulfhydryl and amino cofunctionalized mesoporous silica nanoparticles (Dox/SH/NH<sub>2</sub>-MSNs), into one system through the disulfide bond exchange reaction.<sup>46</sup> After intravenous injection, the generated nanoparticles (Dox/HHS-MSNs) preferentially accumulated at the tumor tissues upon the enhanced permeability and retention (EPR) effect and then were internalized via the specific

**Scheme 1. Schematic Design of Dox/HHS-MSNs for Active Targeting, Endo-Lysosomal Escape, and Multilevel Drug Release to Reverse Cancer MDR<sup>a</sup>**



<sup>a</sup>Panel a shows the construction of Dox/HHS-MSNs by integrating two modules of HA-His-SS-Py and SH/NH<sub>2</sub>-MSNs through disulfide bond exchange reaction. Panel b shows the mechanism of enzyme/redox-triggered multilevel drug release relying on the structural change of Dox/HHS-MSNs. I, Accumulation of Dox/HHS-MSNs at the tumor tissues; II, specific binding to the CD44 receptors on MCF-7/ADR cells; III, CD44-mediated endocytosis and HA degradation by HAase accompanied by some Dox release; IV, endo-lysosomal escape; V, GSH-triggered Dox further release in cytoplasm; VI, getting inside nucleus of released Dox and reversing the MDR eventually.

interaction with CD44 receptors overexpressed on the surface of Dox-resistant human breast adenocarcinoma (MCF-7/ADR) cells. Subsequently, the Dox/HHS-MSNs were transported into the endolysosomes, where the HA derivative shell was subjected to partial degradation accompanied by some Dox release. Note that besides the catabolic enzymes, the intracellular pH gradient in endolysosomes (pH 4.5–5.5) and cytoplasm (pH 7.4) also affects the weak base drugs including Dox transport rates to their sites of action,<sup>47,48</sup> so the introduction of histidine moieties to facilitate the endolysosomal escape was very essential. In the cytosol, the disulfide bonds between HA derivatives and SH/NH<sub>2</sub>-MSNs were ruptured under the high concentration of GSH,<sup>49</sup> followed by the separating of them along with the Dox further release. In the end, the released Dox entered the nucleus and induced the MDR cell apoptosis by intercalating the nuclear DNA.

## 2. EXPERIMENTAL SECTION

**2.1. Materials.** Doxorubicin hydrochloride (Dox-HCl) was bought from Huafeng United Technology Co., Ltd. (Beijing, China). Hyaluronic acid (HA, 11 kDa) was obtained from Freda Biochem Co., Ltd. (Shandong, China). Sodium alginate (SA), cetyltrimethylammonium bromide (CTAB), (3-aminopropyl)triethoxysilane (APTES), tetraethyl orthosilicate (TEOS), and triethylamine (TEA) were bought from Sinopharm Chemical Reagent Co., Ltd. (Shanghai, China). *N*-Hydroxysuccinimide (NHS) and  $\gamma$ -mercaptopyrroltrimethoxysilane (MPTMS) were obtained from Aladdin Biological Technology Co., Ltd. (Shanghai, China). Trypsin (Gibco) and RPMI 1640 medium (1640, Gibco) were obtained from Pufei Biotechnology Co., Ltd. (Shanghai, China). 3-(4,5-dimethylthiazol-2-yl)-2,5-diphenyltetrazolium bromide (MTT), fetal bovine serum (FBS), and penicillin-streptomycin solution (Hyclone) were purchased from SunShine Biotechnology Co., Ltd. (Nanjing, China). Lyso Tracker Green and 1,1'-diocadecyl-3,3,3',3'-tetramethylindotricarbocyanine iodide (DiR) were obtained from Life Technologies.

**2.2. Synthesis of SH/NH<sub>2</sub>-MSNs.** SH/NH<sub>2</sub>-MSNs were synthesized by reference to a literature with slight modification.<sup>50</sup> Specifically, 1.0 g of CTAB was dissolved in 480 mL of pure water and then 0.28 g of NaOH was added. The mixture solution was heated up to 80 °C, followed by the injection of 5.0 mL of TEOS with 1.0 mL/min under vigorous stirring. After that, 2.6 mmol of MPTMS and APTES were immediately added to achieve 8.7:1:1 (TEOS: MPTMS: APTES, *n*: *n*: *n*). The mixture was continuously stirred for 2 h and the white product was separated by centrifugation at 12000 g for 10 min. The product was then transferred into a flask and refluxed in a mixture solution containing 150 mL of methanol and 5.0 mL of concentrated hydrochloric acid to remove CTAB. Furthermore, the product was washed with pure water and methanol alternately. Finally, the clean SH/NH<sub>2</sub>-MSNs were obtained after vacuum drying.

**2.3. Preparation of Dox/HHS-MSNs.** Dox as the model drug was obtained by alkylating Dox-HCl with two equivalents of TEA in DMSO for 12 h. Two hundred microliters of DMSO solution of Dox (5 mg/mL) was incubated with 2.0 mL of Hepes buffer (pH 8.0) containing 5.0 mg of SH/NH<sub>2</sub>-MSNs. After incubation for 12 h in the dark, Dox/SH/NH<sub>2</sub>-MSNs were centrifuged at 12000 g for 10 min. Then, Dox/SH/NH<sub>2</sub>-MSNs were washed with pure water thoroughly to remove the free Dox. In order to prepare Dox/HHS-MSNs, 5.0 mg of HA-His-SS-Py (Scheme S1) was first hydrated in pure water overnight to allow swelling and complete solubilization. Then 4.0 mg of Dox/SH/NH<sub>2</sub>-MSNs dispersed in pure water were added into the HA-His-SS-Py solution. After stirring for 6 h, Dox/HHS-MSNs were centrifuged and washed with pure water to dislodge the unconnected HA derivatives. Finally, Dox/HHS-MSNs were dried using the freezing dryer (Christ Alpha 2–4 LD plus, John Morris Scientific) for future use. As contrast formulations, multifunctional HA derivatives conjugated Dox/SH/NH<sub>2</sub>-MSNs through amide bonds (Dox/HH-MSNs) and sodium alginate (SA) derivatives conjugated Dox/SH/NH<sub>2</sub>-MSNs through disulfide bonds (Dox/SHS-MSNs) were also

constructed, which contained the histidine moieties likewise. The synthetic procedures were described in SI.

**2.4. Characterization.** The hydrodynamic size and zeta potential of different preparations were measured using a Brookhaven Analyzer (Holtville, USA). For transmission electron microscopy (TEM) imaging, the samples were observed using a JEM-2100F microscopy (JEOL, JAPAN) at 200 kV potential. Nitrogen adsorption–desorption analysis was recorded through a Micromeritics ASAP2050 system at 77 K and the powder samples were degassed for 12 h at 373 K before the measurements. The nonlocal density functional theory (NLDFT) and Brunauer–Emmett–Teller (BET) methods were used to determine the pore size distributions and specific surface areas, respectively. The quantification of –SH and –NH<sub>2</sub> functionalized on SH/NH<sub>2</sub>-MSNs were described in SI using the Ellman's method<sup>51</sup> and fluorescamine method,<sup>52</sup> respectively. The Gel permeation chromatography (GPC) system (Shimadzu Co., JAPAN) was used to determine the amount of HA-His-SS-Py capping on SH/NH<sub>2</sub>-MSNs, which contained a LC-20A pump, a RID-10A refractive index detector and a LC solution software. A TSK-gel G4000PW<sub>XL</sub> column (300 mm × 7.8 mm, Tosoh Co., Japan) was employed. 0.1 M sodium nitrate was designated as the mobile phase. The amount of Dox was determined using a HPLC system (Shimadzu Co., JAPAN), which contained a LC-20AB pump, a RF-10AXL fluorescence detector and a LC solution software. An InertSustain C18 column (250 mm × 4.6 mm, 5  $\mu$ m, GL Sciences Inc.) was employed. The excitation and emission wavelength of Dox were set at 496 and 553 nm, respectively. The composition of mobile phase was methanol, water and acetic acid at 65:35:2 (v: v: v).

**2.5. In Vitro Study of HAase and GSH Triggered Dox Release.** The dialysis method was employed to study the Dox release from different formulations in vitro. Simply, 500  $\mu$ L of the aqueous suspensions of Dox/SH/NH<sub>2</sub>-MSNs, Dox/HHS-MSNs, Dox/HH-MSNs, and Dox/SHS-MSNs (1 mg of Dox) were added into the respective dialysis bag (MWCO 14 kDa) against 25 mL of different buffer solution with different concentrations of HAase and GSH at 37 °C under stirring at 100 rpm. 500  $\mu$ L aliquot of each release medium was taken out at predetermined time points and replaced with equivoluminal fresh medium. The amount of Dox released was assayed using HPLC.

**2.6. Cell Culture.** MCF-7/ADR and MCF-7 cells obtained from Cell Bank of Chinese Academy of Sciences (Shanghai, China) were cultivated in 1640 medium with 15% and 10% (v: v) FBS, respectively. Besides, 100  $\mu$ g/mL streptomycin and 100 U/mL penicillin were added into the above medium. The cells were cultivated in an incubator (Thermo Scientific, USA) with 90% relative humidity and 5% CO<sub>2</sub> at 37 °C.

**2.7. Study of Cellular Uptake and Endocytosis Pathways.** MCF-7/ADR cells in 24-well plates at  $1 \times 10^5$  cells/well were cultured in 1640 medium for 24 h. Next, the culture medium was discarded and different preparations with Dox concentration of 10  $\mu$ g/mL were added for 1, 2, 4, 6, and 8 h of incubation to investigate time-dependent uptake. After discarding the supernatant, cold PBS was added to wash cells thrice. Then, 200  $\mu$ L of lysis buffer was incubated with the cells in each well for 30 min. The samples were centrifuged at 1800 g for 5 min and 20  $\mu$ L aliquot of supernatant was pipetted to assay the content of cell protein using the Pierce BCA protein assay kit. 100  $\mu$ L of mixed solvents of acetonitrile: methanol (2:1, v:v) containing 2% (v:v) concentrated HCl were mixed with the residual samples to extract the Dox thoroughly and the amount was assayed using HPLC. The cellular uptake of Dox was calculated as the following equation.<sup>53</sup> Uptake of Dox ( $\mu$ g/mg) =  $Q_{\text{Dox}}/Q_{\text{cellproteins}}$  where  $Q_{\text{Dox}}$  and  $Q_{\text{cellproteins}}$  were the amounts of Dox and cell proteins, respectively. To investigate the concentration-dependent uptake, different preparations with Dox concentration in the range of 1–20  $\mu$ g/mL were added into the given wells for 4 h of incubation. The same processing steps were followed as above to calculate the Dox uptake.

The free HA competitive inhibitory test was carried out to estimate the active targeting role of HA derivatives. Different concentrations of free HA was first added to the 24-well plates for 1 h of incubation with the MCF-7/ADR and MCF-7 cells, which were CD44-overexpressed

and CD44-deficient, respectively. Then different preparations containing 10  $\mu\text{g}/\text{mL}$  of Dox were added for additional 4 h of incubation with the cells in the retention of free HA. The cell protein content and the Dox amount was assayed as above. The cellular uptake without HA was used as control.

To investigate the cellular uptake mechanism, different inhibitors for specific pathways were incubated with the MCF-7/ADR cells in given wells for 1 h of incubation, among which sucrose (154 mg/mL), nystatin (15  $\mu\text{g}/\text{mL}$ ), amiloride (133  $\mu\text{g}/\text{mL}$ ) and sodium azide (0.1%, w:v) were inhibitors of clathrin, caveolin, macropinocytosis and energy mediated endocytosis, respectively. Next, different preparations containing 10  $\mu\text{g}/\text{mL}$  of Dox were added for additional 4 h of incubation in the retention of various inhibitors. The cell protein content and Dox amount were assayed as above. The cellular uptake without inhibitors was used as control.

**2.8. Endo-Lysosomal Escape Activity.** MCF-7/ADR cells in confocal microscopy dishes at  $1 \times 10^5$  cells/dish were cultured for 24 h. Then, different preparations containing 5  $\mu\text{g}/\text{mL}$  of Dox were added for 2 h of incubation. After that, the cold PBS was added to each dish to wash the cells thrice. Subsequently, fresh medium without FBS was incubated with the cells for another 0 and 4 h. Then, the cells were stained using 1  $\mu\text{g}/\text{mL}$  of Hoechst 33342 (Beyotime Biotechnology, China) for 15 min and 500 nM of Lyso-Tracker Green for 30 min. Finally, the stained cells after being washed with cold PBS were detected using confocal laser scanning microscopy (CLSM).

**2.9. Cell Apoptosis and Cytotoxicity.** The Annexin V-FITC/PI Apoptosis Detection Kit (Vazyme Biotech, Nanjing) was used for detection of MCF-7/ADR cell apoptosis. The cells in 6-well plates at  $1 \times 10^5$  cells/well were cultured for 24 h. Then, the medium containing different preparations with 5  $\mu\text{g}/\text{mL}$  of Dox was incubated with the cells for 12 h. Then, the processing and staining of cell samples were conducted following the operating instructions. The samples were analyzed using the flow cytometry (BD AccuriC6, USA).

The cytotoxicity of different blank and Dox-loaded preparations was estimated using the MTT assay. MCF-7/ADR cells in 96-well plates at  $1 \times 10^4$  cells/well were cultured for 24 h. Next, different preparations containing the same Dox concentration of 0.1–20  $\mu\text{g}/\text{mL}$  and blank preparations were added for 24 and 48 h of incubation with the cells. Afterward, 20  $\mu\text{L}$  of the MTT solution (5 mg/mL) was incubated with the cells in each well for another 4 h. Then, 150  $\mu\text{L}$  of DMSO was mixed with the cells after discarding the supernatant. The UV absorbance intensity at 570 nm was determined by a microplate reader (Thermo Electron Corporation, USA).

**2.10. Animals and Tumor Xenograft Models.** The female BALB/c nude mice (18–25 g) and male Sprague–Dawley (SD) rats (180–220 g) obtained from the Veterinary College of Yangzhou

University (Jiangsu, China) were treated according to the Guide for Care and Use of Laboratory Animals in China Pharmaceutical University. To construct the MCF-7/ADR tumor xenograft model,  $2 \times 10^7$  cells were inoculated in the right back of nude mice. The tumor volume ( $V$ ) was measured by a vernier caliper and the formula of  $V = L \times W^2/2$  was applied, in which  $L$  was the longest diameter and  $W$  was the shortest diameter perpendicular to length.

**2.11. In Vivo Study of Pharmacokinetics and Biodistribution.** Twenty-four SD rats were divided into four groups ( $n = 6$ ) randomly and then injected with different formulations intravenously. The injection dosage of Dox was 5 mg/kg. At predetermined time points, the blood samples were drawn and 100  $\mu\text{L}$  of mixed solvents of acetonitrile: methanol (2:1, v:v) containing 2% (v:v) concentrated HCl were added into 100  $\mu\text{L}$  of each sample. After vortex for 30 min, the mixture were centrifuged at 12000 g for 5 min. Twenty microliters of supernatant was injected into the HPLC system.

The noninvasive in vivo imaging technique was used to explore the biodistribution of different preparations in MCF-7/ADR tumor-bearing mice. DiR was a lipophilic near-infrared fluorescent probe and loaded into HHS-MSNs, HH-MSNs and SHS-MSNs in accordance with the method of loading paclitaxel into MSNs.<sup>54</sup> When the tumor size was 100–200  $\text{mm}^3$ , the mice were injected with DiR/HHS-MSNs, DiR/HH-MSNs and DiR/SHS-MSNs intravenously. The injection dosage of DiR was 5 mg/kg. At predefined time points, the mice were anesthetized and imaged rapidly through the Maestro in vivo imaging instruments. After 24 h postinjection, the main organs and tumors were harvested from the euthanized mice for ex vivo imaging. The above tissues were circled and marked as region-of-interest (ROI). The DiR intensity in ROI was determined by the software of Maestro 3.

**2.12. In Vivo Antitumor Efficacy.** The mice with about 50  $\text{mm}^3$  of tumor volume were divided into 5 groups ( $n = 6$ ) randomly,<sup>14</sup> and then injected with different preparations intravenously for day 0, 2, 4, 6, and 8. Each injection dosage was 5 mg/kg. The body weight and tumor volume were monitored every second day for 14 days. At last day, the tumors along with the organs (hearts, livers, spleens, lungs, and kidneys) were collected from the euthanized mice and washed with saline several times. Then, the above tissues were fixed with 10% formalin and embedded in paraffin. Finally, the paraffin sections were stained with hematoxylin and eosin (HE) dyes and observed through an optical microscope.

**2.13. Statistical Analysis.** The type of mean  $\pm$  SD was applicable to the results and one-way ANOVA or two-tailed Student's  $t$  test was used to test the statistical significance. \* $P < 0.05$ , \*\* $P < 0.01$ , and \*\*\* $P < 0.001$  represented significance, high significance and extreme significance, respectively.

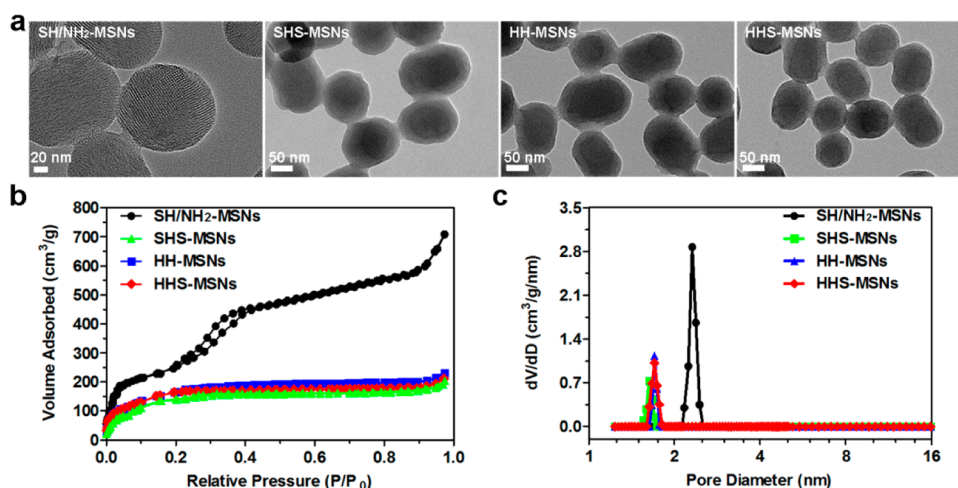


**Figure 1.** (a) TEM images of SH/NH<sub>2</sub>-MSNs (first from left), SHS-MSNs (second from left), HH-MSNs (second from right) and HHS-MSNs (first from right), (b) N<sub>2</sub> adsorption/desorption isotherms, and (c) pore size distribution curves of SH/NH<sub>2</sub>-MSNs, SHS-MSNs, HH-MSNs, and HHS-MSNs.

### 3. RESULTS AND DISCUSSION

**3.1. Preparation and Characterization of Dox/HHS-MSNs.** The Dox/HHS-MSNs were fabricated as follows. First, HA-His-SS-Py was synthesized and characterized through  $^1\text{H}$  NMR. The grafting ratio of His-SS-Py linked to HA under optimal conditions was  $24.7 \pm 3.1\%$  ( $n = 3$ ). As another module, SH/ $\text{NH}_2$ -MSNs as the inorganic drug-storing cores were synthesized using the co-condensation method, which brought about the homogeneous distribution of  $-\text{SH}$  and  $-\text{NH}_2$  on the surface of SH/ $\text{NH}_2$ -MSNs.<sup>55,56</sup> The quantitative study of  $-\text{SH}$  and  $-\text{NH}_2$  on SH/ $\text{NH}_2$ -MSNs showed that  $525.91 \mu\text{mol}$  of  $-\text{SH}$  and  $296.24 \mu\text{mol}$  of  $-\text{NH}_2$  were grafted onto 1 g of SH/ $\text{NH}_2$ -MSNs, which could ensure enough HA derivatives to be covalently grafted onto MSNs and the positive charge of MSNs. The synthetic SH/ $\text{NH}_2$ -MSNs had uniform spherical structures and their average diameter was about 140 nm as shown in TEM images (Figure 1a).

Next, the Dox was encapsulated into the channels of SH/ $\text{NH}_2$ -MSNs. Then the negatively charged HA-His-SS-Py covalently bound to the surface of SH/ $\text{NH}_2$ -MSNs, which led to an obvious charge reversion from about +16 mV of SH/ $\text{NH}_2$ -MSNs to  $-32$  mV of Dox/HHS-MSNs (Table S1). The eventual entrapment efficiency and drug loading ratio were  $85.9 \pm 0.5\%$  and  $25.6 \pm 0.1\%$ , respectively ( $n = 3$ ). The hydrodynamic size of Dox/HHS-MSNs showed no remarkable change in three different media of water, pH 7.4 PBS and 50% serum over 24 h, proving the excellent colloidal stability of Dox/HHS-MSNs (Figure S1).

To determine the amounts of HA derivatives grafted on SH/ $\text{NH}_2$ -MSNs, the supernatants were collected during the preparation of Dox/HHS-MSNs by centrifugation, and then monitored by the GPC system. As shown in Figure S2, the GPC chromatogram indicated a good separating degree of HA derivatives from other substances with retention time at 8.42 min. The grafting ratio of HA derivatives was about 6.37% of the total

mass of Dox/HHS-MSNs. The TEM examination (Figure 1a) displayed the uniform spherical structures and homogeneous polymer shells of Dox/HHS-MSNs, as well as other two contrast formulations, Dox/HH-MSNs and Dox/SHS-MSNs. The nitrogen ( $\text{N}_2$ ) isothermal adsorption/desorption and pore size distribution curves of bare SH/ $\text{NH}_2$ -MSNs, SHS-MSNs, HH-MSNs and HHS-MSNs were presented in Figure 1b and c. The BET surface area ( $S_{\text{BET}}$ ), average pore diameter ( $D_p$ ) and total pore volume ( $V_t$ ) were summarized in Table S2. After different grafting, the above parameter values of HHS-MSNs, HH-MSNs, and SHS-MSNs were obviously reduced compared to SH/ $\text{NH}_2$ -MSNs, indicating that the internal MSNs were enshrouded by the outer polymers commendably.

**3.2. In Vitro Study of HAase/GSH-Triggered Drug Release.** To simulate the Dox release from Dox/HHS-MSNs under intracellular conditions, the dialysis bag diffusion method was applied in pH 7.4 Hepes buffer with different concentrations of HAase and GSH (Figure 2). As a control group, most of drugs were released from Dox/SH/ $\text{NH}_2$ -MSNs within 6 h under different pH medium. Conversely, Dox/HHS-MSNs, Dox/HH-MSNs and Dox/SHS-MSNs exhibited the sustained release property and no more than 20% of the encapsulated Dox was released into the pH 7.4 medium without HAase and GSH simultaneously for 48 h, implying that the polymer shell of HA or SA derivatives exerted a powerful influence on preventing the premature drug release. However, in the presence of HAase (0.5 mg/mL), up to 40% of the Dox was released from Dox/HHS-MSNs and Dox/HH-MSNs, which was owned to the degradation of HA derivatives by HAase. Besides, about 30% of the Dox from Dox/SHS-MSNs and Dox/HHS-MSNs was released into the medium containing 10 mM GSH on account of the breakage of disulfide bonds along with the departure of HA or SA derivatives from the surface of SH/ $\text{NH}_2$ -MSNs. Furthermore, the cumulative Dox-releasing amount from Dox/HHS-MSNs was improved to 55%

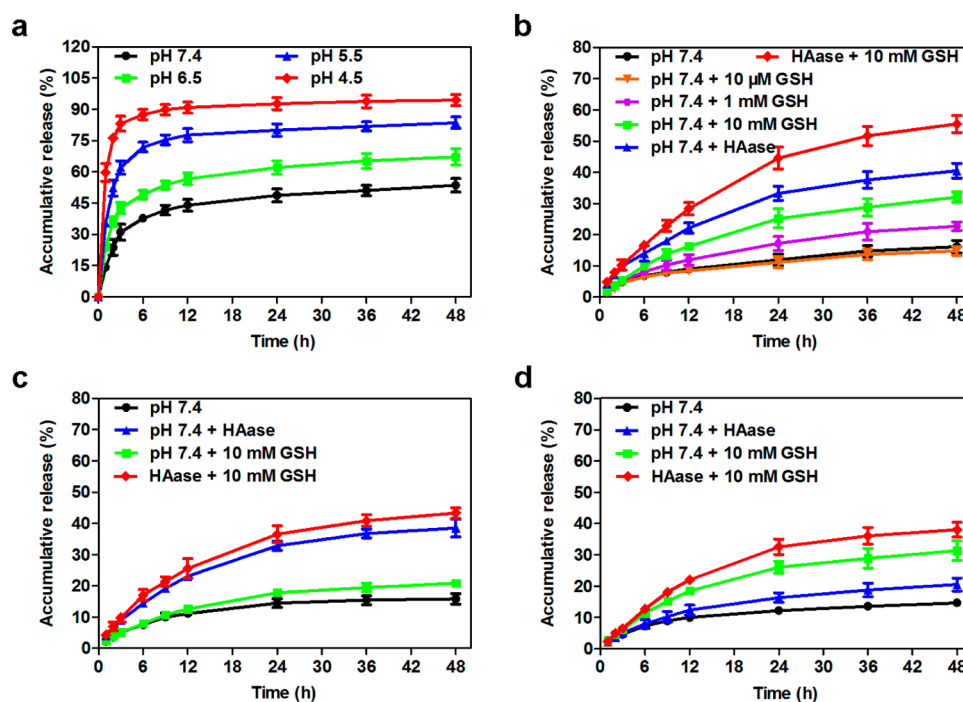


**Figure 2.** In vitro Dox-releasing profiles of (a) Dox/SH/ $\text{NH}_2$ -MSNs under different pH mediums over time, (b) Dox/HHS-MSNs, (c) Dox/HH-MSNs, and (d) Dox/SHS-MSNs under pH 7.4 medium containing different concentrations of HAase and GSH over time.

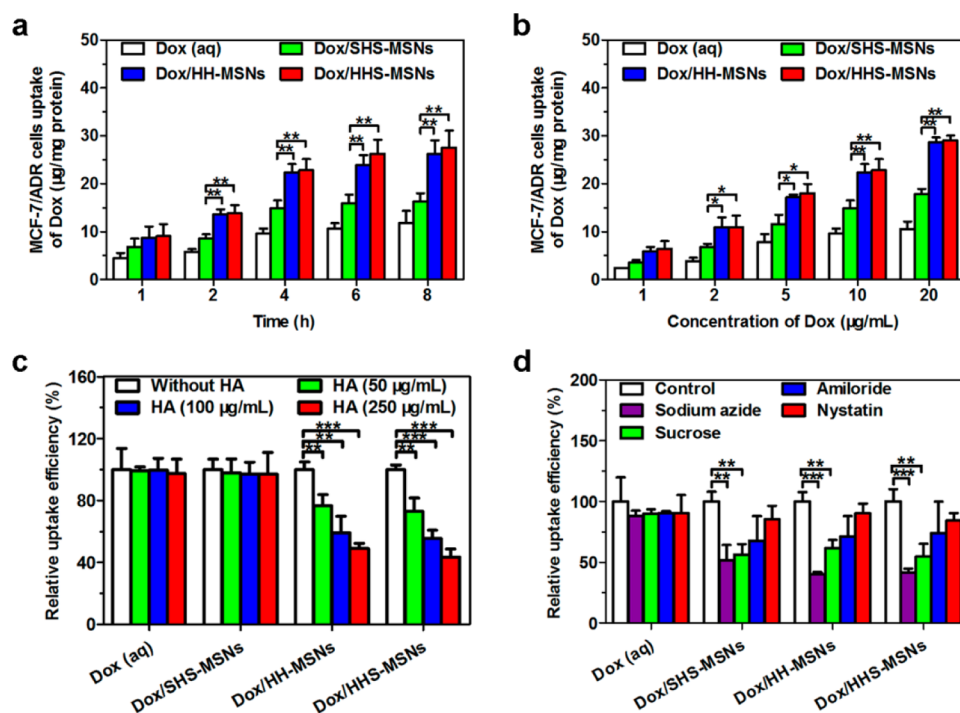


**Figure 3.** (a, b) MCF-7/ADR cellular uptake of Dox from free Dox solution, Dox/SHS-MSNs, Dox/HH-MSNs and Dox/HHS-MSNs (a) under different incubation time with 10  $\mu\text{g/mL}$  of Dox and (b) under different Dox concentrations for 4 h. \* $P < 0.05$ , \*\* $P < 0.01$ . (c, d) Relative MCF-7/ADR cellular uptake efficiency of Dox from Dox solution, Dox/SHS-MSNs, Dox/HH-MSNs, Dox/HHS-MSNs with 10  $\mu\text{g/mL}$  of Dox for 4 h (c) under different concentrations of free HA and (d) under various endocytosis inhibitors. \*\* $P < 0.01$ , \*\*\* $P < 0.001$ .

in the presence of HAase and 10 mM GSH simultaneously, which indicated that the combination of HAase and GSH could trigger a more efficient Dox release. These results suggested that the multilevel drug release effect could lead to more drug release inside cells and easier reaching of the effective therapeutic concentration for reversing the MDR.

**3.3. Study of Cellular Uptake and Endocytosis Pathways.** To evaluate the cellular uptake, the CD44-overexpressed MCF-7/ADR cells were used. As displayed in Figure 3a, the cellular uptake was time-dependent and all the formulations based on MSNs presented a higher cellular uptake of Dox than Dox solution, confirming that free Dox molecules could barely get inside MCF-7/ADR cells due to the efflux function of the P-gp. The cellular uptake from Dox/HHS-MSNs and Dox/HH-MSNs showed no significant difference, but was higher than that from Dox/SHS-MSNs, which proved that the CD44-mediated endocytosis could promote the cellular uptake. In addition, the cellular uptake was Dox concentration-dependent and the tendency was similar to that for time-dependent diagram above (Figure 3b).

To further prove the specific interaction between HA and CD44, the cellular uptake from different preparations was compared on CD44-deficient MCF-7 cells and CD44-overexpressed MCF-7/ADR cells. To block the CD44-mediated pathway, different concentrations of free HA were preincubated with the cells above. The relative uptake efficiency of Dox after pretreatment with HA was comparable to that without HA pretreatment on MCF-7 cells (Figure S3, while Dox/HHS-MSNs and Dox/HH-MSNs showed an apparent decline on MCF-7/ADR cells in a HA concentration-dependent manner (Figure 3c). The results confirmed that Dox/HHS-MSNs and Dox/HH-MSNs could be endocytosed by MCF-7/ADR cells through the CD44-mediated pathway.

Next, to understand the mechanism of MCF-7/ADR cellular uptake from different preparations, various endocytosis inhibitors were used to block the corresponding uptake pathways (Figure 3d). Both sodium azide and sucrose could significantly decrease the cellular uptake from Dox/HHS-MSNs, Dox/HH-MSNs and Dox/SHS-MSNs, which indicated that the three formulations above entered cells via active transport and mainly through the clathrin-mediated pathway. It meant that the formulations based on MSNs would be transported into endolysosomes inevitably after internalization, which was a major barrier against the intracellular delivery.<sup>12</sup>

**3.4. Intracellular Endolysosomal Escape Behavior.** The intracellular endolysosomal escape behaviors of different preparations were observed in MCF-7/ADR cells by CLSM. As presented in Figure 4, a large area of yellow fluorescence ascribing to the overlap of red Dox fluorescence and green Lyso-Tracker fluorescence was observed from the merged images of Dox/HHS-MSNs, Dox/HH-MSNs, and Dox/SHS-MSNs at 2 h, which indicated that the three formulations were stranded in the endolysosomes. As prolonging incubation periods to 6 h, the Dox signals from Dox/HHS-MSNs, Dox/HH-MSNs, and Dox/SHS-MSNs were distinctly separated from the LysoTracker signals, which demonstrated that the three formulations successfully escaped from endolysosomes relying on the proton sponge effect of histidine moieties grafted on HA and SA derivatives. To further validate the role of histidine moieties, the proton buffering experiment was tested using the acid–base titration method (Figure S4). Compared to the physical mixture of SH/NH<sub>2</sub>-MSNs and HA, the histidine-containing nanoparticles including HHS-MSNs, HH-MSNs and SHS-MSNs showed a much better proton buffering capacity when the environmental pH was adjusted to acid from neutral, thus further explaining why Dox/HHS-MSNs,

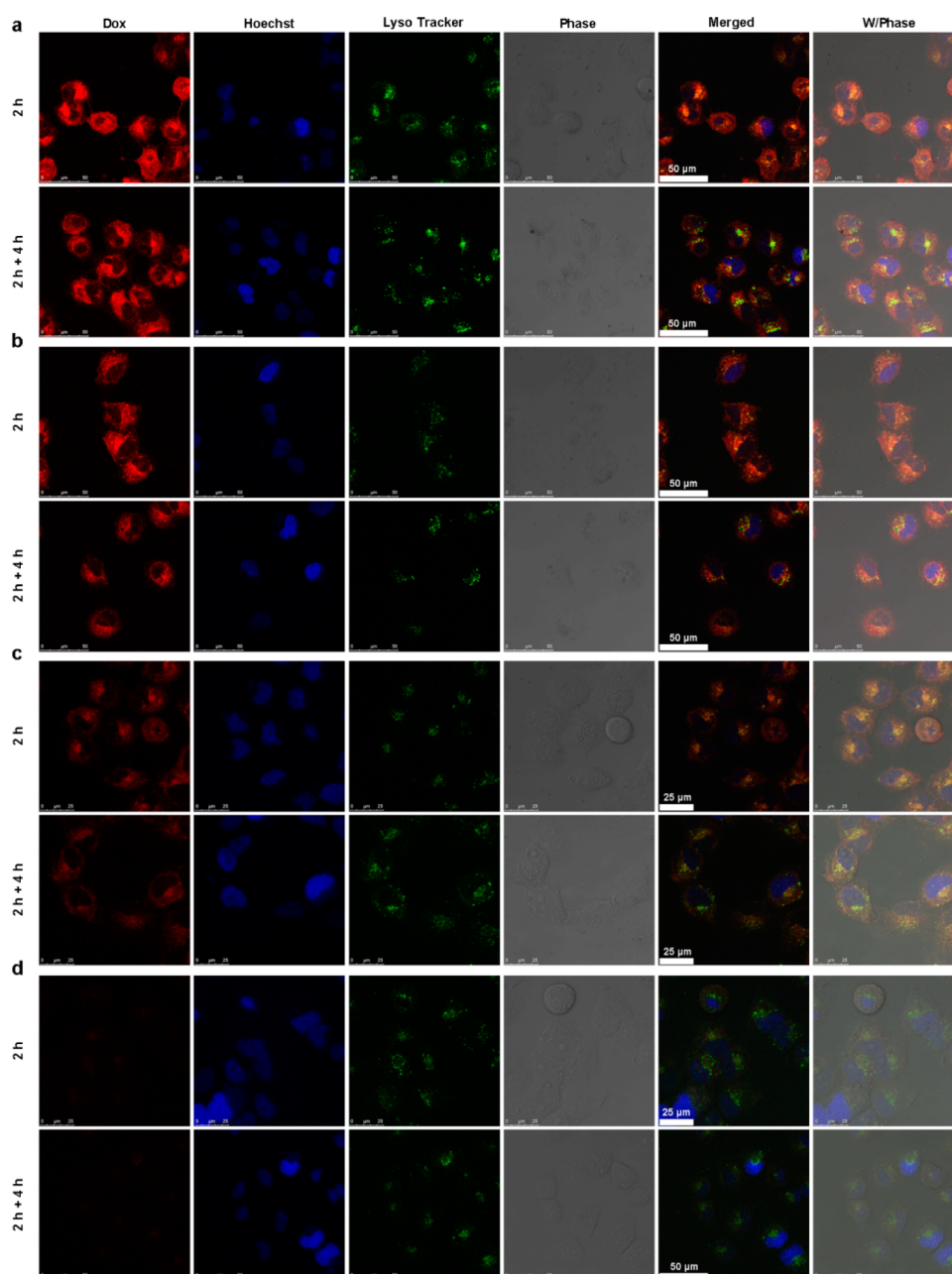


**Figure 4.** CLSM images of MCF-7/ADR cells after incubation with (a) Dox/HHS-MSNs, (b) Dox/HH-MSNs, (c) Dox/SHS-MSNs, and (d) free Dox solution for 2 and 6 h. The Dox was observed as red fluorescence. The stained nucleus with Hoechst 33342 were observed as blue fluorescence. The stained lysosomes and late endosomes with Lyso Tracker Green were observed as green fluorescence.

Dox/HH-MSNs and Dox/SHS-MSNs possessed the capability of endolysosomal escape.

**3.5. Cell Apoptosis and Cytotoxicity.** The apoptosis-inducing ability of Dox/HHS-MSNs was first estimated by employing the Annexin V-FITC/PI apoptosis detection kit. As shown in Figure 5a, the total apoptotic ratio of MCF-7/ADR cells after 12 h of incubation with Dox/HHS-MSNs was 37.7%, significantly higher than 26.4% of Dox/HH-MSNs, 17.2% of Dox/SHS-MSNs, and 7.5% of free Dox solution. Afterward, the cytotoxicity of Dox/HHS-MSNs toward MCF-7/ADR cells was assayed using the MTT method. Dox/HHS-MSNs showed a higher cytotoxicity than the other preparations (Figure 5b-5c). The 50% inhibitory concentration ( $IC_{50}$ ) of Dox/HHS-MSNs at 24 h was  $2.75 \pm 0.11 \mu\text{g/mL}$ . As time prolonging to 48 h, the  $IC_{50}$  decreased to  $1.65 \pm 0.09 \mu\text{g/mL}$ , which was about

0.53-fold, 0.30-fold, and 0.11-fold that of Dox/HH-MSNs ( $3.09 \pm 0.24 \mu\text{g/mL}$ ), Dox/SHS-MSNs ( $5.49 \pm 0.27 \mu\text{g/mL}$ ) and the free Dox solution ( $14.86 \pm 0.35 \mu\text{g/mL}$ ), respectively. Nevertheless, the blank formulations did not present obvious cytotoxicity even in a very high concentration (Figure S6). Accordingly, the Dox/HHS-MSNs had the strongest ability to induce apoptosis and cytotoxicity toward MCF-7/ADR cells due to the combined effects of enhanced cellular uptake, endolysosomal escape and efficient multilevel drug release inside cells.

**3.6. Pharmacokinetics and Biodistribution.** To evaluate the pharmacokinetic properties of different preparations in the rats, the blood concentration versus time curves (Figure 6a) were made and their relevant parameters (Table S3) were summarized. Dox/HHS-MSNs exhibited the similar pharmacokinetic behavior to Dox/HH-MSNs, but improved bioavailability than

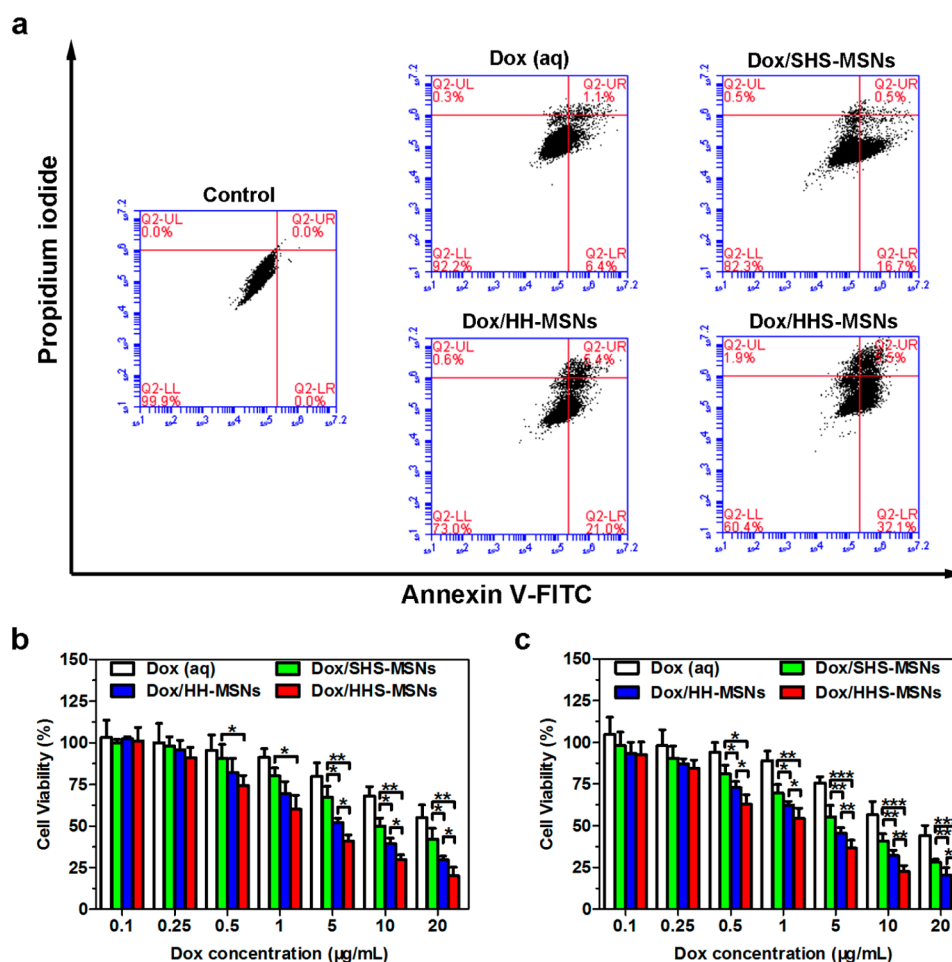


**Figure 5.** (a) Flow cytometry apoptosis scatterplot of MCF-7-ADR cells after 12 h of incubation with Dox solution, Dox/SHS-MSNs, Dox/HH-MSNs, and Dox/HHS-MSNs. (b, c) In vitro cytotoxicity toward MCF-7/ADR cells after incubation with Dox solution, Dox/SHS-MSNs, Dox/HH-MSNs, and Dox/HHS-MSNs for (b) 24 and (c) 48 h. \* $P < 0.05$ , \*\* $P < 0.01$ , \*\*\* $P < 0.001$ .

Dox/SHS-MSNs and free Dox solution, which was substantiated by a greater area under the curve (AUC), longer half-time ( $t_{1/2}$ ) and lower clearance (Cl). The possible reason was concerned with the unique properties of alginate itself, such as the strong bioadhesive performance, easy cross-linking and gathering in the presence of bivalent cations.<sup>57</sup> It meant that more Dox/HHS-MSNs could be transported to the tumor site and then exerted therapeutic action.

To detect the biodistribution of different preparations through in vivo imaging system, they were first labeled with DiR, a near-infrared fluorescent probe, and then injected into the tumor-bearing mice intravenously. As presented in Figure 6b, the DiR signals from DiR/HHS-MSNs were captured at 1 h and continued up to 24 h postinjection, which was comparable to that from DiR/HH-MSNs, but stronger than that from DiR/SHS-MSNs at all time points. Similarly, for ex vivo imaging, the DiR signals from the harvested tumors after injection with DiR/HHS-MSNs and DiR/HH-MSNs for 24 h were also significantly higher than that after injection with DiR/SHS-MSNs (Figure 6c). The quantitative DiR intensity in ROI further proved the preminent tumor-targeting efficiency of DiR/HHS-MSNs and DiR/HH-MSNs through the combination of the inherent EPR effect and acquired active targeting (Figure 6d). This enhanced targeting effect could facilitate more drug-loaded nanoparticles to arrive at the tumor tissues and eventually achieve more preferable MDR reversing effect.

**3.7. In Vivo Antitumor Efficacy.** The MCF-7/ADR tumor-bearing mice receiving successive administration with different preparations were used to evaluate in vivo antitumor efficacy. In Figure 7a, all Dox-loaded preparations displayed different degrees of inhibiting effects on tumor volume when compared to saline. Among them, Dox/HHS-MSNs and Dox/HH-MSNs exhibited a stronger tumor inhibition capability than Dox/SHS-MSNs and free Dox solution, which owed to the superior pharmacokinetic behaviors and active-targeting properties of HA derivative shells. However, Dox/HHS-MSNs showed a more efficient inhibitory effect than Dox/HH-MSNs, suggesting that the superior intracellular Dox release could reinforce the antitumor activity. In addition, the typical tumor images vividly displayed the greatest shrinkage from the mice injected with Dox/HHS-MSNs (Figure 7b). Compared to the saline group, no obvious weight change was found in the treatment with Dox/HHS-MSNs, Dox/HH-MSNs, and Dox/SHS-MSNs except for free Dox group (Figure 7c). The histological analysis of HE-stained tumor section from Dox/HHS-MSNs group showed a better remission than that from other groups, which further proved the prominent antitumor efficacy of Dox/HHS-MSNs (Figure 7d). These in vivo results confirmed that the tumor suppression effects of nanoparticles depend upon their overall physicochemical properties mainly including the core/shell structures. Although the MSNs as the drug reservoirs have widely been investigated

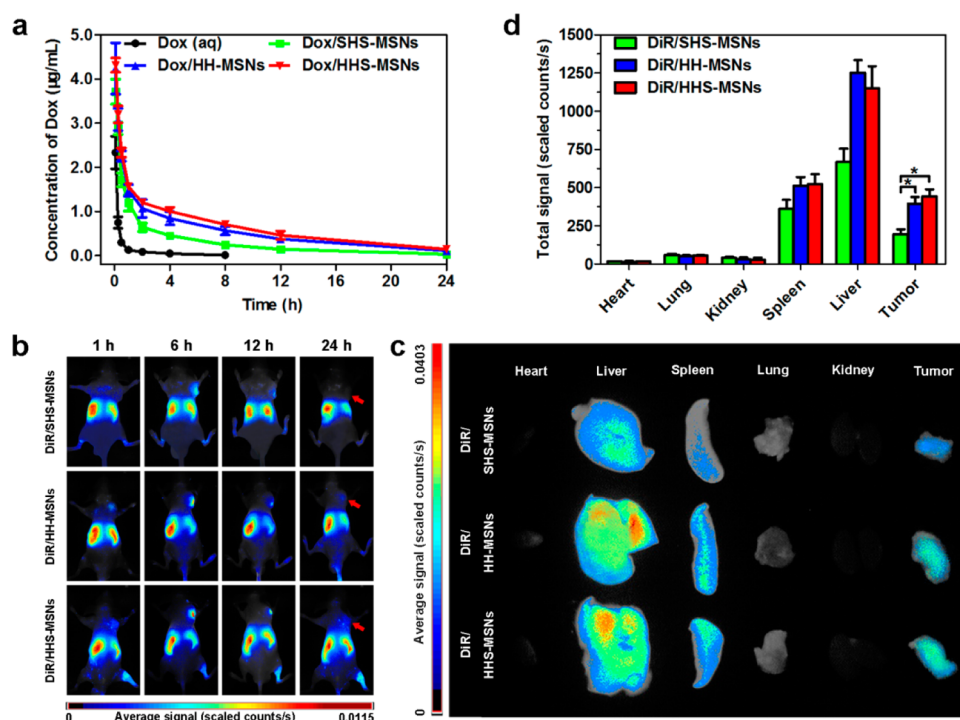


**Figure 6.** (a) Blood concentration versus time curves from the rats injected with different preparations including free Dox solution, Dox/SHS-MSNs, Dox/HH-MSNs, and Dox/HHS-MSNs. (b) The biodistribution of DiR/SHS-MSNs (top), DiR/HH-MSNs (middle), and DiR/HHS-MSNs (bottom) in mice detected through in vivo imaging system. The tumor regions were indicated by red arrows. (c) Ex vivo tissue images from the mice injected with DiR/SHS-MSNs (top), DiR/HH-MSNs (middle), and DiR/HHS-MSNs (bottom) at 24 h. (d) DiR intensity of different tissues from the mice injected with DiR/SHS-MSNs, DiR/HH-MSNs, and DiR/HHS-MSNs at 24 h. \* $P < 0.05$ .

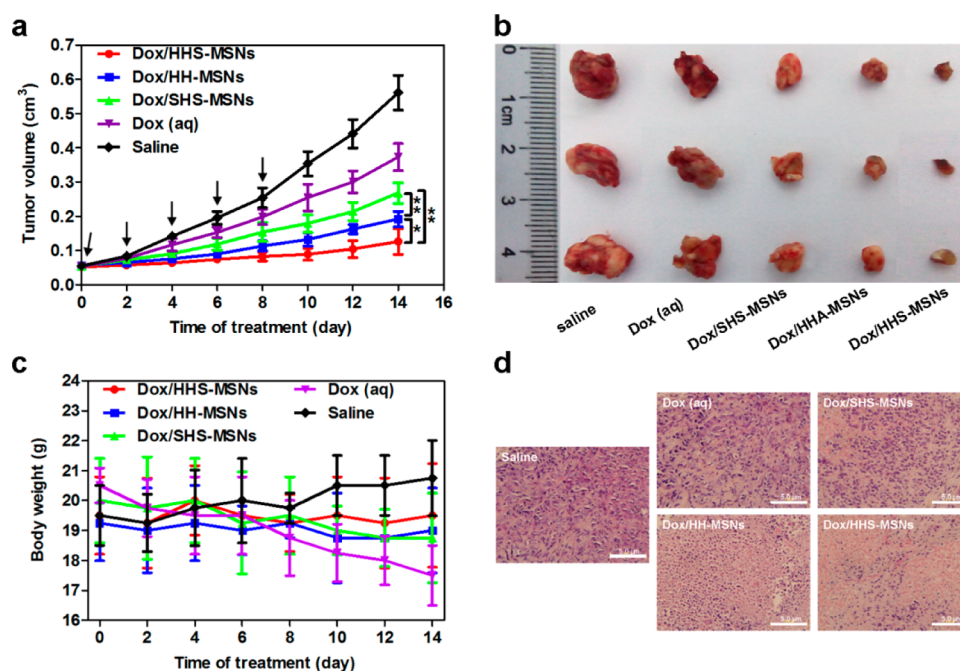


**Figure 7.** (a) Tumor growth curves from different groups of nude mice treated with saline, free Dox solution, Dox/SHS-MSNs, Dox/HH-MSNs, Dox/HHS-MSNs at day 0, 2, 4, 6, and 8. The Dox dosage was 5 mg/kg. \* $P < 0.05$ , \*\* $P < 0.01$ . (b) Representative tumor images from the mice treated with saline, free Dox solution, Dox/SHS-MSNs, Dox/HH-MSNs and Dox/HHS-MSNs. (c) Weight changes of the mice during treatment with different preparations. (d) Represent images of tumor tissues stained with HE from the groups of saline, free Dox solution, Dox/SHS-MSNs, Dox/HH-MSNs, and Dox/HHS-MSNs. Scale bar in each image is 5 µm.

in many papers, the capping agents including polymer shells had powerful influences on the main performance of DDSs. For this study, a high therapeutic effect on MDR cancer could

be obtained in consequence of the enhanced cellular uptake, rapid endolysosomal escape, and sufficient intracellular multi-level drug release.

## 4. CONCLUSIONS

In summary, we developed a novel enzyme and redox dual-responsive anticancer DDS based on two modules, SH/NH<sub>2</sub>-MSNs and HA-His-SS-Py. The introduction of HA-His-SS-Py polymer shell greatly improved a series of properties of Dox/HHS-MSNs both in vitro and in vivo, such as plasma stability, targeting ability, bioavailability and antitumor efficacy. The designed nanocarrier rendered intracellular multilevel drug release characteristics correlated to HAase and GSH levels, which could release the maximum encapsulated Dox in the simultaneous presence of high levels of two stimuli. Our results suggested that the combination of EPR effect and active targeting did facilitate the nanoparticles into the tumor cells; in addition, the efficient drug release inside cells was also important in the successful cancer chemotherapy. It needed to be stressed that our nanocarrier possessed the function of endolysosomal escape, which could assist the drug to conquer the intracellular barrier and reach the site of action. Eventually, we accomplished the expected goal by designing an intelligent DDS based on the physiologic and pathologic characteristics to reverse the MDR phenomenon in cancer treatment.

## ■ ASSOCIATED CONTENT

### Supporting Information

The Supporting Information is available free of charge on the ACS Publications website at DOI: 10.1021/acsami.6b04885.

Synthesis of HA-His-SS-Py, SA-His-SS-Py, and HA-His-Bn; the quantification of -SH and -NH<sub>2</sub> on SH/NH<sub>2</sub>-MSNs; the preparation of Dox/SHS-MSNs and Dox/HH-MSNs; Schemes S1–S2; Tables S1–S3; and Figures S1–S6 (PDF)

## ■ AUTHOR INFORMATION

### Corresponding Authors

\*E-mail: szg707@126.com.

\*E-mail: zhangcan@cpu.edu.cn.

### Notes

The authors declare no competing financial interest.

## ■ ACKNOWLEDGMENTS

This work was supported by the National Natural Science Foundation of China (81273468, 81473153, 81503006, 81503003), National Basic Research Program of China (2015CB755500), National Science Foundation of Jiangsu Province of China (BK20140672, BK20150698), Fundamental Research Funds for the Central Universities of China (2015PY014), and 111 Project from the Ministry of Education of China and the State Administration of Foreign Expert Affairs of China (No. 111-2-07).

## ■ REFERENCES

- (1) Siegel, R.; Naishadham, D.; Jemal, A. Cancer Statistics, 2013. *Ca-Cancer J. Clin.* **2013**, *63* (1), 11–30.
- (2) Bouwman, P.; Jonkers, J. The Effects of Deregulated DNA Damage Signalling on Cancer Chemotherapy Response and Resistance. *Nat. Rev. Cancer* **2012**, *12* (9), 587–598.
- (3) Holohan, C.; Van Schaeybroeck, S.; Longley, D. B.; Johnston, P. G. Cancer Drug Resistance: An Evolving Paradigm. *Nat. Rev. Cancer* **2013**, *13* (10), 714–726.
- (4) Nooter, K.; Stoter, G. Molecular Mechanisms of Multidrug Resistance in Cancer Chemotherapy. *Pathol., Res. Pract.* **1996**, *192* (7), 768–780.
- (5) Shukla, S.; Ohnuma, S.; Ambudkar, S. V. Improving Cancer Chemotherapy with Modulators of ABC Drug Transporters. *Curr. Drug Targets* **2011**, *12* (5), 621.
- (6) Yin, Q.; Shen, J.; Zhang, Z.; Yu, H.; Li, Y. Reversal of Multidrug Resistance by Stimuli-Responsive Drug Delivery Systems for Therapy of Tumor. *Adv. Drug Delivery Rev.* **2013**, *65* (13–14), 1699–1715.
- (7) Kirtane, A. R.; Kalscheuer, S. M.; Panyam, J. Exploiting Nanotechnology to Overcome Tumor Drug Resistance: Challenges and Opportunities. *Adv. Drug Delivery Rev.* **2013**, *65* (13), 1731–1747.
- (8) Kreuzaler, P.; Watson, C. J. Killing a Cancer: What Are the Alternatives? *Nat. Rev. Cancer* **2012**, *12* (6), 411–424.
- (9) Dong, X.; Mumper, R. J. Nanomedicinal Strategies to Treat Multidrug-Resistant Tumors: Current Progress. *Nanomedicine* **2010**, *5* (4), 597–615.
- (10) Su, Z.; Chen, M.; Xiao, Y.; Sun, M.; Zong, L.; Asghar, S.; Dong, M.; Li, H.; Ping, Q.; Zhang, C. ROS-Triggered and Regenerating Anticancer Nanosystem: An Effective Strategy to Subdue Tumor's Multidrug Resistance. *J. Controlled Release* **2014**, *196*, 370–383.
- (11) Duan, X.; Xiao, J.; Yin, Q.; Zhang, Z.; Yu, H.; Mao, S.; Li, Y. Smart pH-Sensitive and Temporal-Controlled Polymeric Micelles for Effective Combination Therapy of Doxorubicin and Disulfiram. *ACS Nano* **2013**, *7* (7), 5858–5869.
- (12) Xu, X.; Zhang, L.; Assanhou, A. G.; Wang, L.; Zhang, Y.; Li, W.; Xue, L.; Mo, R.; Zhang, C. Acid/Redox Dual-Activated Liposomes for Tumor-Targeted Drug Delivery and Enhanced Therapeutic Efficacy. *RSC Adv.* **2015**, *5* (83), 67803–67808.
- (13) Jiang, T.; Mo, R.; Bellotti, A.; Zhou, J.; Gu, Z. Gel-Liposome-Mediated Co-Delivery of Anticancer Membrane-Associated Proteins and Small-Molecule Drugs for Enhanced Therapeutic Efficacy. *Adv. Funct. Mater.* **2014**, *24* (16), 2295–2304.
- (14) Mo, R.; Jiang, T.; DiSanto, R.; Tai, W.; Gu, Z. ATP-Triggered Anticancer Drug Delivery. *Nat. Commun.* **2014**, *5*, 3364.
- (15) Jiao, Y.; Sun, Y.; Chang, B.; Lu, D.; Yang, W. Redox- and Temperature-Controlled Drug Release from Hollow Mesoporous Silica Nanoparticles. *Chem. - Eur. J.* **2013**, *19* (45), 15410–15420.
- (16) Mackowiak, S. A.; Schmidt, A.; Weiss, V.; Argyo, C.; Von Schirnding, C.; Bein, T.; Bräuchle, C. Targeted Drug Delivery in Cancer Cells with Red-Light Photoactivated Mesoporous Silica Nanoparticles. *Nano Lett.* **2013**, *13* (6), 2576–2583.
- (17) Park, S. M.; Kim, M. S.; Park, S. J.; Park, E. S.; Choi, K. S.; Kim, Y. S.; Kim, H. R. Novel Temperature-Triggered Liposome with High Stability: Formulation, in Vitro Evaluation, and in Vivo Study Combined with High-Intensity Focused Ultrasound (Hifu). *J. Controlled Release* **2013**, *170* (3), 373–379.
- (18) Lee, S. F.; Zhu, X. M.; Wang, Y. X.; Xuan, S. H.; You, Q.; Chan, W. H.; Wong, C. H.; Wang, F.; Yu, J. C.; Cheng, C. H.; Leung, K. C. Ultrasound, pH, and Magnetically Responsive Crown-Ether-Coated Core/Shell Nanoparticles as Drug Encapsulation and Release Systems. *ACS Appl. Mater. Interfaces* **2013**, *5* (5), 1566–1574.
- (19) Kwon, I. C.; Bae, Y. H.; Kim, S. W. Electrically Credible Polymer Gel for Controlled Release of Drugs. *Nature* **1991**, *354*, 291–293.
- (20) Saito, G.; Swanson, J. A.; Lee, K. D. Drug Delivery Strategy Utilizing Conjugation Via Reversible Disulfide Linkages: Role and Site of Cellular Reducing Activities. *Adv. Drug Delivery Rev.* **2003**, *55* (2), 199–215.
- (21) Lu, N.; Tian, Y.; Tian, W.; Huang, P.; Liu, Y.; Tang, Y.; Wang, C.; Wang, S.; Su, Y.; Zhang, Y.; Pan, J.; Teng, Z.; Lu, G. Smart Cancer Cell Targeting Imaging and Drug Delivery System by Systematically Engineering Periodic Mesoporous Organosilica Nanoparticles. *ACS Appl. Mater. Interfaces* **2016**, *8* (5), 2985–2993.
- (22) Qu, Q.; Ma, X.; Zhao, Y. Targeted Delivery of Doxorubicin to Mitochondria Using Mesoporous Silica Nanoparticle Nanocarriers. *Nanoscale* **2015**, *7* (40), 16677–16686.
- (23) Barbe, C.; Bartlett, J.; Kong, L.; Finnie, K.; Lin, H. Q.; Larkin, M.; Calleja, S.; Bush, A.; Calleja, G. Silica Particles: A Novel Drug-Delivery System. *Adv. Mater.* **2004**, *16* (21), 1959–1966.
- (24) Lai, C.-Y.; Trewyn, B. G.; Jeftinija, D. M.; Jeftinija, K.; Xu, S.; Jeftinija, S.; Lin, V. S.-Y. A Mesoporous Silica Nanosphere-Based

Carrier System with Chemically Removable Cds Nanoparticle Caps for Stimuli-Responsive Controlled Release of Neurotransmitters and Drug Molecules. *J. Am. Chem. Soc.* **2003**, *125* (15), 4451–4459.

(25) Wang, X.; Chen, H.; Zheng, Y.; Ma, M.; Chen, Y.; Zhang, K.; Zeng, D.; Shi, J. Au-Nanoparticle Coated Mesoporous Silica Nanocapsule-Based Multifunctional Platform for Ultrasound Mediated Imaging, Cytoclastosis and Tumor Ablation. *Biomaterials* **2013**, *34* (8), 2057–2068.

(26) Wang, Y.; Wang, K.; Zhao, J.; Liu, X.; Bu, J.; Yan, X.; Huang, R. Multifunctional Mesoporous Silica-Coated Graphene Nanosheet Used for Chemo-Photothermal Synergistic Targeted Therapy of Glioma. *J. Am. Chem. Soc.* **2013**, *135* (12), 4799–4804.

(27) Giri, S.; Trewyn, B. G.; Stellmaker, M. P.; Lin, V. S. Y. Stimuli-Responsive Controlled-Release Delivery System Based on Mesoporous Silica Nanorods Capped with Magnetic Nanoparticles. *Angew. Chem., Int. Ed.* **2005**, *44* (32), 5038–5044.

(28) Porta, F.; Lamers, G. E. M.; Zink, J. I.; Kros, A. Peptide Modified Mesoporous Silica Nanocontainers. *Phys. Chem. Chem. Phys.* **2011**, *13* (21), 9982–9985.

(29) Wu, X.; Wang, Z.; Zhu, D.; Zong, S.; Yang, L.; Zhong, Y.; Cui, Y. pH and Thermo Dual-Stimuli-Responsive Drug Carrier Based on Mesoporous Silica Nanoparticles Encapsulated in a Copolymer-Lipid Bilayer. *ACS Appl. Mater. Interfaces* **2013**, *5* (21), 10895–10903.

(30) Salis, A.; Fanti, M.; Medda, L.; Nairi, V.; Cugia, F.; Piludu, M.; Sogos, V.; Monduzzi, M. Mesoporous Silica Nanoparticles Functionalized with Hyaluronic Acid and Chitosan Biopolymers. Effect of Functionalization on Cell Internalization. *ACS Biomater. Sci. Eng.* **2016**, *2* (5), 741–751.

(31) Zhang, J.; Yuan, Z.-F.; Wang, Y.; Chen, W.-H.; Luo, G.-F.; Cheng, S.-X.; Zhuo, R.-X.; Zhang, X.-Z. Multifunctional Envelope-Type Mesoporous Silica Nanoparticles for Tumor-Triggered Targeting Drug Delivery. *J. Am. Chem. Soc.* **2013**, *135* (13), 5068–5073.

(32) Luo, Z.; Cai, K.; Hu, Y.; Zhao, L.; Liu, P.; Duan, L.; Yang, W. Mesoporous Silica Nanoparticles End-Capped with Collagen: Redox-Responsive Nanoreservoirs for Targeted Drug Delivery. *Angew. Chem., Int. Ed.* **2011**, *50* (3), 640–643.

(33) Luo, Z.; Ding, X.; Hu, Y.; Wu, S.; Xiang, Y.; Zeng, Y.; Zhang, B.; Yan, H.; Zhang, H.; Zhu, L.; et al. Engineering a Hollow Nanocontainer Platform with Multifunctional Molecular Machines for Tumor-Targeted Therapy in Vitro and in Vivo. *ACS Nano* **2013**, *7* (11), 10271–10284.

(34) Pan, L.; He, Q.; Liu, J.; Chen, Y.; Ma, M.; Zhang, L.; Shi, J. Nuclear-Targeted Drug Delivery of Tat Peptide-Conjugated Monodisperse Mesoporous Silica Nanoparticles. *J. Am. Chem. Soc.* **2012**, *134* (13), 5722–5725.

(35) Toole, B. P. Hyaluronan: From Extracellular Glue to Pericellular Cue. *Nat. Rev. Cancer* **2004**, *4* (7), 528–539.

(36) Stern, R. Hyaluronan Catabolism: A New Metabolic Pathway. *Eur. J. Cell Biol.* **2004**, *83* (7), 317–325.

(37) Toole, B. P. Hyaluronan-CD44 Interactions in Cancer: Paradoxes and Possibilities. *Clin. Cancer Res.* **2009**, *15* (24), 7462–7468.

(38) Götte, M.; Yip, G. W. Heparanase, Hyaluronan, and CD44 in Cancers: A Breast Carcinoma Perspective. *Cancer Res.* **2006**, *66* (21), 10233–10237.

(39) Bertrand, P.; Girard, N.; Duval, C.; d'Anjou, J.; Chauzy, C.; Ménard, J. F.; Delpuch, B. Increased Hyaluronidase Levels in Breast Tumor Metastases. *Int. J. Cancer* **1997**, *73* (3), 327–331.

(40) Midoux, P.; Pichon, C.; Yaouanc, J. J.; Jaffrès, P. A. Chemical Vectors for Gene Delivery: A Current Review on Polymers, Peptides and Lipids Containing Histidine or Imidazole as Nucleic Acids Carriers. *Br. J. Pharmacol.* **2009**, *157* (2), 166–178.

(41) Chen, Y.; Yang, W.; Chang, B.; Hu, H.; Fang, X.; Sha, X. In Vivo Distribution and Antitumor Activity of Doxorubicin-Loaded N-Isopropylacrylamide-Co-Methacrylic Acid Coated Mesoporous Silica Nanoparticles and Safety Evaluation. *Eur. J. Pharm. Biopharm.* **2013**, *85* (3), 406–412.

(42) Huang, I. P.; Sun, S. P.; Cheng, S. H.; Lee, C. H.; Wu, C. Y.; Yang, C. S.; Lo, L. W.; Lai, Y. K. Enhanced Chemotherapy of Cancer

Using pH-Sensitive Mesoporous Silica Nanoparticles to Antagonize P-Glycoprotein-Mediated Drug Resistance. *Mol. Cancer Ther.* **2011**, *10* (5), 761–769.

(43) Ma, M.; Chen, H.; Chen, Y.; Zhang, K.; Wang, X.; Cui, X.; Shi, J. Hyaluronic Acid-Conjugated Mesoporous Silica Nanoparticles: Excellent Colloidal Dispersity in Physiological Fluids and Targeting Efficacy. *J. Mater. Chem.* **2012**, *22* (12), 5615.

(44) Chen, Z.; Li, Z.; Lin, Y.; Yin, M.; Ren, J.; Qu, X. Bioresponsive Hyaluronic Acid-Capped Mesoporous Silica Nanoparticles for Targeted Drug Delivery. *Chem. - Eur. J.* **2013**, *19* (5), 1778–1783.

(45) Yu, M.; Jambhrunkar, S.; Thorn, P.; Chen, J.; Gu, W.; Yu, C. Hyaluronic Acid Modified Mesoporous Silica Nanoparticles for Targeted Drug Delivery to Cd44-Overexpressing Cancer Cells. *Nanoscale* **2013**, *5* (1), 178–183.

(46) van der Vlies, A. J.; O'Neil, C. P.; Hasegawa, U.; Hammond, N.; Hubbell, J. A. Synthesis of Pyridyl Disulfide-Functionalized Nanoparticles for Conjugating Thiol-Containing Small Molecules, Peptides, and Proteins. *Bioconjugate Chem.* **2010**, *21* (4), 653–662.

(47) Fan, S.; Niu, Y.; Tan, N.; Wu, Z.; Wang, Y.; You, H.; Ke, R.; Song, J.; Shen, Q.; Wang, W.; et al. Lss2 Enhances Chemosensitivity of Breast Cancer by Counteracting Acidic Tumor Microenvironment through Inhibiting Activity of V-ATPase Proton Pump. *Oncogene* **2013**, *32* (13), 1682–1690.

(48) Borges, R.; Domínguez, N.; Estévez-Herrera, J.; Pereda, D.; Machado, J. D. Vesicular Ca<sup>2+</sup> Mediates Granule Motion and Exocytosis. *Cell Calcium* **2012**, *51* (3), 338–341.

(49) Wang, Y. C.; Wang, F.; Sun, T. M.; Wang, J. Redox-Responsive Nanoparticles from the Single Disulfide Bond-Bridged Block Copolymer as Drug Carriers for Overcoming Multidrug Resistance in Cancer Cells. *Bioconjugate Chem.* **2011**, *22* (10), 1939–1945.

(50) Wani, A.; Muthuswamy, E.; Savithra, G. H.; Mao, G.; Brock, S.; Oupicky, D. Surface Functionalization of Mesoporous Silica Nanoparticles Controls Loading and Release Behavior of Mitoxantrone. *Pharm. Res.* **2012**, *29* (9), 2407–2418.

(51) Ellman, G. L. Tissue Sulfhydryl Groups. *Arch. Biochem. Biophys.* **1959**, *82* (1), 70–77.

(52) Ritter, H.; Nieminen, M.; Karppinen, M.; Brühwiler, D. A Comparative Study of the Functionalization of Mesoporous Silica MCM-41 by Deposition of 3-Aminopropyltrimethoxysilane from Toluene and from the Vapor Phase. *Microporous Mesoporous Mater.* **2009**, *121* (1–3), 79–83.

(53) Mo, R.; Sun, Q.; Li, N.; Zhang, C. Intracellular Delivery and Antitumor Effects of pH-Sensitive Liposomes Based on Zwitterionic Oligopeptide Lipids. *Biomaterials* **2013**, *34* (11), 2773–2786.

(54) Jia, L.; Shen, J.; Li, Z.; Zhang, D.; Zhang, Q.; Liu, G.; Zheng, D.; Tian, X. In Vitro and in Vivo Evaluation of Paclitaxel-Loaded Mesoporous Silica Nanoparticles with Three Pore Sizes. *Int. J. Pharm.* **2013**, *445* (1–2), 12–19.

(55) Lu, Y.-K.; Yan, X.-P. An Imprinted Organic-Inorganic Hybrid Sorbent for Selective Separation of Cadmium from Aqueous Solution. *Anal. Chem.* **2004**, *76* (2), 453–457.

(56) Kao, H.-M.; Liao, C.-H.; Palani, A.; Liao, Y.-C. One-Pot Synthesis of Ordered and Stable Cubic Mesoporous Silica SBA-1 Functionalized with Amino Functional Groups. *Microporous Mesoporous Mater.* **2008**, *113* (1), 212–223.

(57) Gombotz, W. R.; Wee, S. F. Protein Release from Alginate Matrices. *Adv. Drug Delivery Rev.* **2012**, *64*, 194–205.